

Flow Simulations for the First Aeroelastic Prediction Workshop Using the EZNSS Code

Daniella E. Raveh¹

Faculty of Aerospace Engineering, Technion - IIT, Haifa 32000, Israel

Yair Mor Yossef² and Yuval Levy³

Israeli CFD Center, Caesarea Industrial Park 38900, Israel

This paper presents numerical simulations that were performed with the EZNSS flow solver for the first NASA Langley Aeroelastic Prediction Workshop. Two configurations were studied, the Benchmark Supercritical Wing (BSCW) and the High Reynolds Number Aerostructural Dynamics (HIRENASD) model. The BSCW wing is a rigid wing that was studied at transonic flow conditions, at a fixed angle of attack. Static as well as time-accurate simulations were performed, using several computational meshes and turbulence models, with the purpose of predicting the pressure coefficient distribution at a wing section at 60% of the span, where pressure data was available from a wind tunnel experiment. All of the models predicted the shock location within 10% chords of its wind-tunnel location. None of the models predicted accurately the pressure recovery behind the shock on the upper and lower surfaces. While some turbulence models and computational setups resulted in a steady flow, some predicted flow unsteadiness, with fluctuations of the shock position and of the aerodynamic coefficient values. This may indicate that the case of the BSCW wing, at the studied flow conditions, is on the verge of buffet instability. The HIRENASD wing was studied for its elastic deformations and associated pressure coefficient distribution at three flow conditions. All of the studied flow conditions resulted in good correlation between the computed and experimental pressure coefficient data. The HIRENASD wing was also excited at its second-bending mode. The transfer function between the pressure

coefficient distribution at different span-wise section and the amplitude of motion of a reference point was computed and compared to experimental data. A fair comparison was demonstrated. Overall, it appears that the numerical simulations predicted well the transonic static aeroelastic response and the response to forced excitation in cases of attached flows. The transonic cases of detached flows behind a shock were found to be highly sensitive to the numerical parameters of the simulation, especially the turbulence model used.

I. Introduction

The accurate computation of aeroelastic responses and unsteady aerodynamic forces due to structural motion is of great importance to aircraft aeroelastic analysis and structural design. The first Aeroelastic Prediction Workshop (AePW), taking after the Drag and High-lift Prediction Workshops, addresses these topics. The AePW aims at assessment of state-of-the-art CFD codes simulating flow-fields about wings undergoing prescribed motions or elastic deformations at transonic flight conditions. Three subject configurations were proposed for evaluation. These include the Rectangular Supercritical Wing (RSW), the Benchmark Supercritical Wing (BSCW) and the High Reynolds Number Aerostructural Dynamics (HIRENASD) model that were presented in [1].

The BSCW, tested in the Transonic Dynamics Tunnel at NASA Langley, is shown in Figure 1. The model is mounted on a large splitter plate, 40 inches off of the wind tunnel wall. The BSCW has a rigid rectangular planform, with a cross-section of the NASA SC(2)-0414 airfoil. Pressure measurements were taken by unsteady pressure transducers at the 60% span station. Boundary layer transition was fixed at 7.5% chord. All data used in this study was obtained at Mach 0.85 and a dynamic pressure of 200 psf, setting the Reynolds number at 4.49 million based on wing chord. Dynamic data was obtained for the BSCW by oscillating the model in a pitching motion about the

¹Senior Lecturer, Faculty of Aerospace Engineering, Technion - IIT, Haifa 32000, Israel, AIAA Senior Member

²Chief Scientist, Israeli CFD Center, Caesarea Industrial Park 38900

³CEO, Israeli CFD Center, Caesarea Industrial Park 38900

30% chord point.

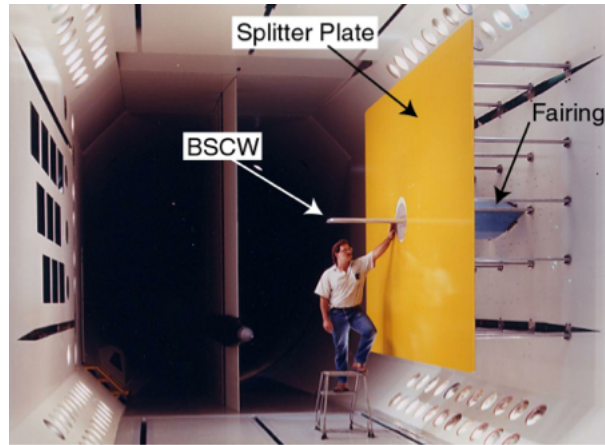


Fig. 1: BSCW mounted in wind-tunnel

The HIRENASD model, tested in the European Transonic Wind (ETW) tunnel, is shown in Figure 2. The model has a 34 degree aft-swept, tapered clean wing, with a BAC 3-11 supercritical wing section. The test article is a semi-span model, ceiling-mounted through a non-contacting fuselage fairing to a turntable, balance, and excitation system. The first two bending modes have frequencies of approximately 27 and 79 Hz; the first torsion mode has a frequency of approximately 265 Hz. The instrumentation includes 259 in-situ unsteady pressure transducers at seven span stations. In addition to the unsteady pressure measurements, balance and acceleration measurements were obtained.

The present paper presents numerical simulations performed with the Elastic Zonal Navier-Stokes Solver (EZNSS) in the framework of the first Aeroelastic Prediction Workshop, of the BSCW and HIRENASD configurations. This paper presents results from steady and unsteady flows, as well as static aeroelastic analyses.

II. Governing Equations

The governing equations are obtained by Favre-averaging the Navier-Stokes equations (RANS) and modeling the Reynolds stress tensor. In what follows, the symbol $(-)$ indicates non-weighted averaging, the symbol (\sim) signifies Favre averaging, and the symbol $('')$ denotes Favre fluctuations. In a compact form, the mean-flow equations may be expressed in generalized coordinates with strong



Fig. 2: HIRENASD mounted in wind-tunnel

conservation-law form as:

$$\frac{\partial \hat{\mathbf{Q}}}{\partial \tau} + \frac{\partial(\hat{\mathbf{F}}^c - \hat{\mathbf{F}}^d)}{\partial \xi} + \frac{\partial(\hat{\mathbf{G}}^c - \hat{\mathbf{G}}^d)}{\partial \eta} + \frac{\partial(\hat{\mathbf{H}}^c - \hat{\mathbf{H}}^d)}{\partial \zeta} = 0 \quad (1)$$

where τ denotes the time and ξ , η , and ζ denote the curvilinear coordinates. The vector $\hat{\mathbf{Q}}$ denotes the mean-flow dependent variables given as:

$$\hat{\mathbf{Q}} = \frac{\mathbf{Q}}{J} = \frac{1}{J} [\bar{\rho}, \bar{\rho} \tilde{u}, \bar{\rho} \tilde{v}, \bar{\rho} \tilde{w}, \bar{E}]^T \quad (2)$$

where J is the Jacobian of the transformation. The fluid density is denoted by ρ , the Cartesian velocity vector components are denoted by u , v , and w , and the total energy is denoted by E . The mean-flow rotated inviscid fluxes are given by:

$$\hat{\mathbf{F}}^c = \frac{1}{J} \begin{bmatrix} \bar{\rho} \tilde{U} \\ \bar{\rho} \tilde{u} \tilde{U} + \xi_x \bar{p} \\ \bar{\rho} \tilde{v} \tilde{U} + \xi_y \bar{p} \\ \bar{\rho} \tilde{w} \tilde{U} + \xi_z \bar{p} \\ (\tilde{E} + \bar{p}) \tilde{U} - \xi_t \bar{p} \end{bmatrix}, \quad \hat{\mathbf{G}}^c = \frac{1}{J} \begin{bmatrix} \bar{\rho} \tilde{V} \\ \bar{\rho} \tilde{u} \tilde{V} + \eta_x \bar{p} \\ \bar{\rho} \tilde{v} \tilde{V} + \eta_y \bar{p} \\ \bar{\rho} \tilde{w} \tilde{V} + \eta_z \bar{p} \\ (\tilde{E} + \bar{p}) \tilde{V} - \eta_t \bar{p} \end{bmatrix}, \quad \hat{\mathbf{H}}^c = \frac{1}{J} \begin{bmatrix} \bar{\rho} \tilde{W} \\ \bar{\rho} \tilde{u} \tilde{W} + \zeta_x \bar{p} \\ \bar{\rho} \tilde{v} \tilde{W} + \zeta_y \bar{p} \\ \bar{\rho} \tilde{w} \tilde{W} + \zeta_z \bar{p} \\ (\tilde{E} + \bar{p}) \tilde{W} - \zeta_t \bar{p} \end{bmatrix} \quad (3)$$

where p denotes the pressure, and U, V , and W denote the Contravariant velocity components given by the relation:

$$\begin{bmatrix} \tilde{U} - \xi_t \\ \tilde{V} - \eta_t \\ \tilde{W} - \zeta_t \end{bmatrix} = \begin{bmatrix} \xi_x & \xi_y & \xi_z \\ \eta_x & \eta_y & \eta_z \\ \zeta_x & \zeta_y & \zeta_z \end{bmatrix} \begin{bmatrix} \tilde{u} \\ \tilde{v} \\ \tilde{w} \end{bmatrix} \quad (4)$$

The mean-flow rotated diffusive flux vectors are given by:

$$\hat{\mathbf{F}}^d = \frac{1}{J} \begin{bmatrix} 0 \\ \xi_i(\bar{\tau}_{ix} - \tilde{\mathfrak{R}}_{ix}) \\ \xi_i(\bar{\tau}_{iy} - \tilde{\mathfrak{R}}_{iy}) \\ \xi_i(\bar{\tau}_{iz} - \tilde{\mathfrak{R}}_{iz}) \\ \xi_i\beta_i \end{bmatrix}, \quad \hat{\mathbf{G}}^d = \frac{1}{J} \begin{bmatrix} 0 \\ \eta_i(\bar{\tau}_{ix} - \tilde{\mathfrak{R}}_{ix}) \\ \eta_i(\bar{\tau}_{iy} - \tilde{\mathfrak{R}}_{iy}) \\ \eta_i(\bar{\tau}_{iz} - \tilde{\mathfrak{R}}_{iz}) \\ \eta_i\beta_i \end{bmatrix}, \quad \hat{\mathbf{H}}^d = \frac{1}{J} \begin{bmatrix} 0 \\ \zeta_i(\bar{\tau}_{ix} - \tilde{\mathfrak{R}}_{ix}) \\ \zeta_i(\bar{\tau}_{iy} - \tilde{\mathfrak{R}}_{iy}) \\ \zeta_i(\bar{\tau}_{iz} - \tilde{\mathfrak{R}}_{iz}) \\ \zeta_i\beta_i \end{bmatrix} \quad (5)$$

where τ_{ij} and $\tilde{\mathfrak{R}}_{ij} = \widetilde{u_i''u_j''}$, are the viscous stress tensor and Reynolds-stress tensor components, respectively. The terms β_i are given as follows:

$$\beta_i = \tilde{u} \left(\bar{\tau}_{ix} - \tilde{\mathfrak{R}}_{ix} \right) + \tilde{v} \left(\bar{\tau}_{iy} - \tilde{\mathfrak{R}}_{iy} \right) + \tilde{w} \left(\bar{\tau}_{iz} - \tilde{\mathfrak{R}}_{iz} \right) + (\bar{\kappa} + \bar{\kappa}_t) \frac{\partial \bar{T}}{\partial x_i} \quad (6)$$

with T denoting the temperature and $\bar{\kappa}$ and $\bar{\kappa}_t$ are the molecular and the turbulent thermal conductivity, respectively. The mean-flow equations are closed using the equation of state for a perfect gas,

$$\bar{p} = (\gamma - 1) \left[\bar{E} - \frac{1}{2} \bar{\rho} (\tilde{u}^2 + \tilde{v}^2 + \tilde{w}^2) \right] \quad (7)$$

where γ is the ratio of specific heats. The unknown Favre-averaging Reynolds stress tensor is modeled in this work using either the Boussinesq hypothesis, via a linear eddy viscosity model, or by using a second moment closure. Two linear eddy viscosity closure models were used in the current work, the two-equation k - ω model developed by Kok [2], also known as the TNT model and is hereto forth referred to as k - ω - TNT , and the Spalart & Allmaras model with Edwards and Chandra modification [3], referred to as SA - EC . The second-moment closure model that is used in the current work was developed by Wilcox [4], and is known as the Stress- ω model, referred herein as RSM - ω . Note that the simple diffusive gradient model that is used in the original Stress- ω model is replaced by the Daly-Harlow [5] diffusive model.

III. Numerical Methods

A. Flow Solver

The governing equations are discretized using a finite difference method on a curvilinear coordinates computational mesh using the Israeli CFD Center (ISCFDC) in-house code, EZNSS. The EZNSS code is a multi-zone Euler/Navier-Stokes flow solver. The code is capable of simulating complex, time-accurate flows about dynamically deforming geometries. This includes relative motion between surfaces as well as deformations caused due to aeroelastic effects. The code contains a number of implicit algorithms and a number of turbulence models. It handles complex geometries using patched grids and the Chimera overset grid topology.

The diffusive fluxes of the mean-flow equations and of the turbulence model equation are discretized using second-order central differencing based on a full-viscous stencil. The convective flux vector of the mean-flow equations may be approximated by second-order central differencing via the Beam & Warming algorithm or by upwind schemes such as the flux vector splitting by Steger-Warming or by an approximate Riemann solver such as the HLLC [6] and the $AUSM^+$ -up scheme [7]. The left and right states of the approximate Riemann solvers are evaluated using a third-order biased MUSCL scheme. The convective flux of the turbulence model is approximated by the HLLC scheme based on the passive scalar approach using a third-order biased MUSCL scheme. The code provides the choice between various implicit time marching schemes for the mean-flow equations, such as the AF-ADI method, the DDADI method [8], and the line Gauss-Seidel method. The time marching scheme that is used for the turbulence models is the unconditionally positive-stable scheme developed by Mor-Yossef and Levy [9, 10]. Second order temporal accuracy is achieved by using dual-time stepping.

B. Aeroelastic Scheme

EZNSS solves the static or dynamic aeroelastic equation of motion (EOM) in modal coordinates. The dynamic EOM reads:

$$[GM]\{\ddot{\xi}\} + [GK]\{\xi\} - \{GF_A(t)\} = 0 \quad (8)$$

and the static EOM reads:

$$[GK]\{\xi\} - \{GF_A(t)\} = 0 \quad (9)$$

where $\{\xi\}$ is the vector of modal deformations, $[GM]$ and $[GK]$ are the generalized mass and stiffness matrices, respectively, and $\{GF_A(t)\}$ is the generalized aerodynamic force vector. The latter is calculated as:

$$\{GF_A(t)\} = [\Phi_A]\{F_A(t)\} \quad (10)$$

where $\{F_A(t)\}$ is the vector of aerodynamic forces provided at the computational surface mesh, and $[\Phi_A]$ is the modal matrix, in which each column holds a structural elastic mode, mapped to the computational surface mesh. The generalized mass and stiffness matrices and the modes matrix are generated by a finite-element code and provided as inputs to the aeroelastic simulation. A spline routine, based on the Infinite Plate Spline (IPS) [11] and beam spline algorithms, is used to map the modes from the finite-element nodes in which they are computed to the CFD surface mesh.

In the dynamic aeroelastic case, the aeroelastic EOM is solved for the generalized displacements following each CFD iteration. In the static case, the static aeroelastic EOM is solved following a user-defined number of CFD iterations, typically in the order of 100. This leads to an efficient aeroelastic scheme in which the elastic shape and the flow solution converge concurrently, while applying only a small number of elastic shape updates. The block-diagram describing the elastic solution procedure is presented in Ref. [12].

Following each solution of the static aeroelastic EOM, the generalized deformations are used to compute the displacements at the computational surface grids, $\{u_A\}$, according to:

$$\{u_A\} = [\Phi_A]\{\xi\} \quad (11)$$

which are then mapped to the whole volume grid using a shearing method [12, 13].

IV. Results and Discussion

A. Benchmark Supercritical Wing (BSCW) Configuration

Flow simulations were conducted at a Mach number of $M_\infty = 0.85$, an angle of attack of $\alpha = 5^\circ$, and at a reference Reynolds number of $Re_\infty = 4.49 \times 10^6$. The test medium in this case is R-134a

and therefore the gas constant γ has been set to 1.116. Two geometry flow models were studied in the present work. In both models, the wind tunnel walls were not modeled and it was assumed that the wing is placed in free-air conditions (with the appropriate experimental flow conditions). The difference between the two flow models lies in the treatment of the large splitter plate (see Figure 1). The first flow model, termed hereafter *configuration 1*, ignores the presence of the large splitter plate, and the computational mesh plane at the wing root (which lies in the same plane as the splitter) is modeled as an inviscid impermeable wall. The second flow model, termed hereafter *configuration 2*, models the splitter that is considered a viscous wall. It should be noted that *configuration 1* follows the gridding guidelines of the first Aeroelastic Prediction Workshop [1], while *configuration 2* does not. The $AUSM^+$ -*up* scheme [7] was used to approximate the mean-flow convective flux.

1. Configuration 1 Simulations

Two computational meshes of a C-O type were studied. A coarse grid with the dimensions of $253 \times 71 \times 99$ in the chord-wise, span-wise, and perpendicular directions, respectively, and a medium mesh of dimensions $361 \times 110 \times 138$ (see Figure 3). For both meshes the far field extends approximately 90 chords away from the wing surface. The first grid point neighboring the wing surface is placed at a distance of 6×10^{-6} wing chords, and 4×10^{-6} wing chords, for the coarse and medium grids, respectively. The simulations were conducted using the $RSM-\omega$, the $SA-EC$, and the $k-\omega-TNT$ turbulence models.

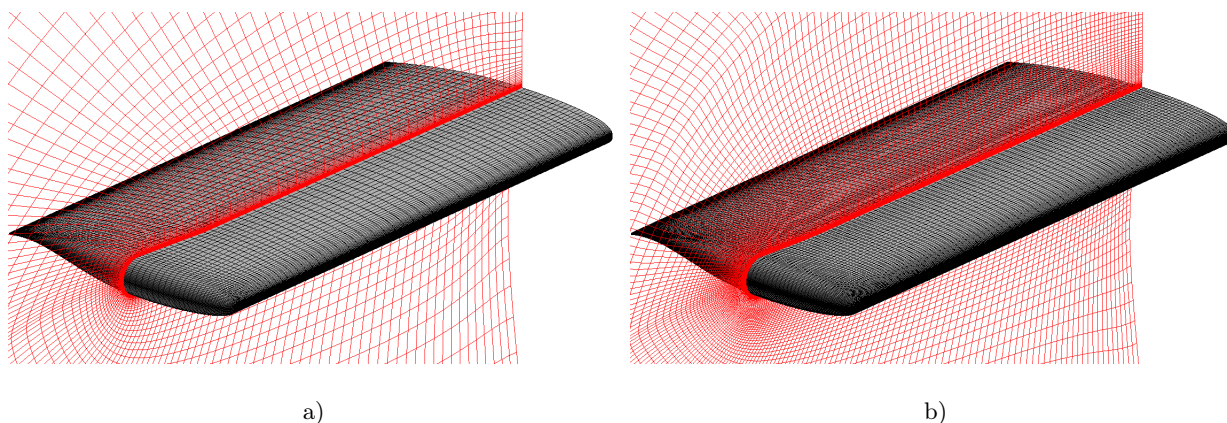
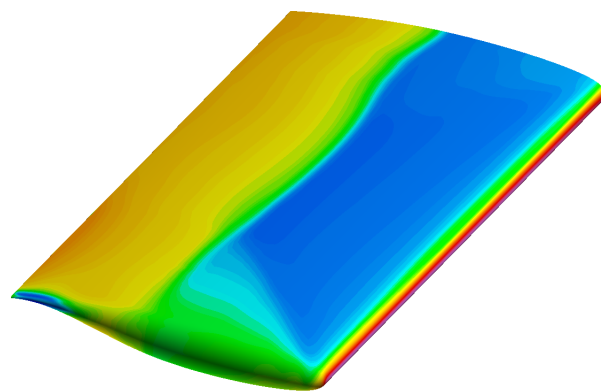


Fig. 3: BSCW *configuration 1* computational mesh; a) coarse grid, b) medium grid

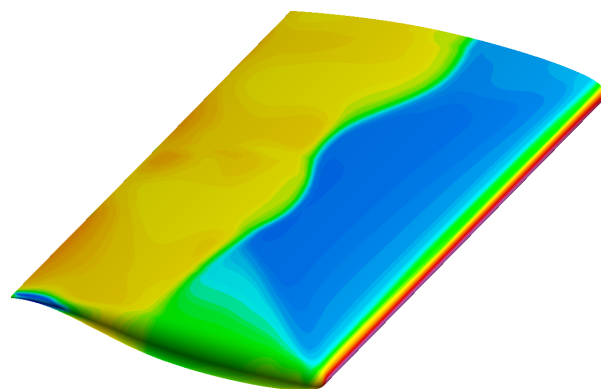
Using the coarse grid, only the $k\text{-}\omega\text{-}TNT$ model reached a converged steady state solution in terms of residual reduction (more than seven orders of magnitude reduction) and aerodynamics forces. The other models did not converge, neither in terms of residual nor in terms of aerodynamic forces, and the flow field exhibited some unsteadiness. Using the medium grid, none of the simulations of the three turbulence models reached a converged solution. The $k\text{-}\omega\text{-}TNT$ resulted in fluctuations of the force coefficients that are of high-frequency and very low-amplitude about a steady condition. For any practical purpose, the force coefficients can be considered to be steady. Time-accurate simulation that were conducted with this model showed no change in the aerodynamics forces.

Figure 4 shows the surface pressure coefficient from the steady simulations using the coarse mesh. A clear difference between the computed results of the span-wise pressure distribution is evident. Using the $k\text{-}\omega\text{-}TNT$ model, the span-wise pressure distribution is nearly uniform from the wing root up to a certain span-wise location toward the wing tip, where downwash effects prevail. On the other-hand, using the $SA\text{-}EC$ and the $RSM\text{-}\omega$ models, the span-wise pressure distribution is non-uniform near the wing root. The reason is that at the wing root these two models predict a stronger separation as compared to the separation predicted by the $k\text{-}\omega\text{-}TNT$ model (not shown). The non-uniform pressure distributions are due to transverse pressure waves, originating from the wing root.

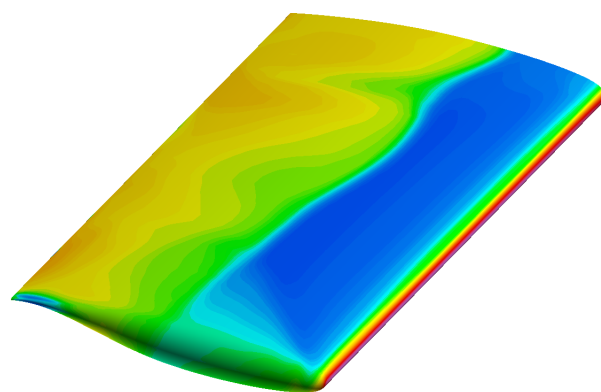
To examine the flow unsteadiness, time-accurate simulations were performed using second-order time accuracy with a normalized physical time step of $\Delta t = 0.01$. At each physical time step twenty sub iterations were used, resulting in a three to four orders of magnitude residual reduction. The initial solutions that were used for the time accurate simulations were the final solutions obtained from the steady flow simulations. The time-accurate results include the $SA\text{-}EC$ model computation using the coarse and medium grids, and the computation from $RSM\text{-}\omega$ model using the coarse grid. Figure 5 shows the time history of the lift coefficient. While the results from the $RSM\text{-}\omega$ model show a clear unsteady flow, the results from the $SA\text{-}EC$ model exhibit a strong decaying oscillation using the coarse grid. On the other hand, the results from the $SA\text{-}EC$ model, using the medium grid, display a clear unsteady flow. This behavior of the lift coefficient obtained from the $SA\text{-}EC$



(a) $k-\omega$ - TNT



(b) $SA-EC$



(c) $RSM-\omega$

Fig. 4: BSCW surface pressure map using the coarse mesh from the steady-state simulations

model is not fully clear and is left for future study.

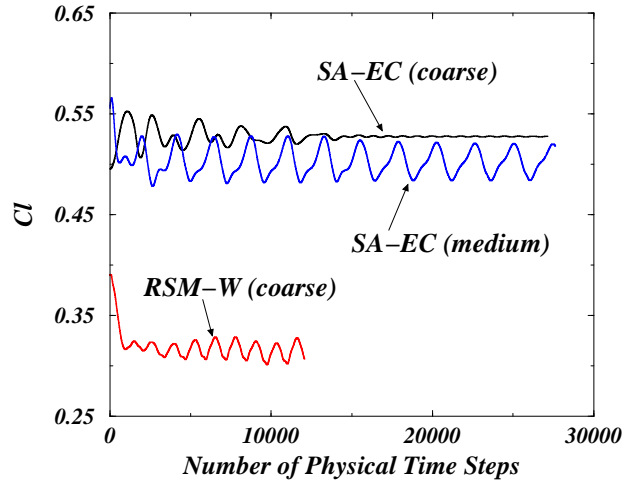
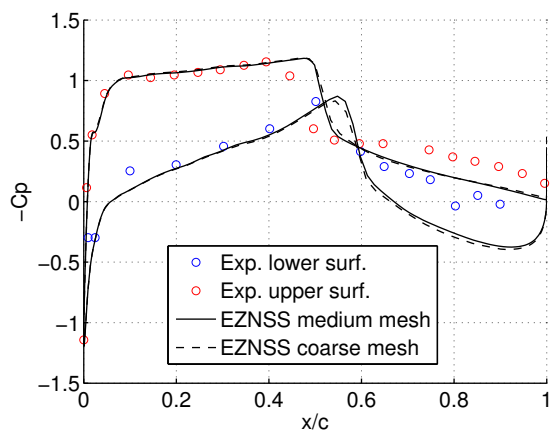


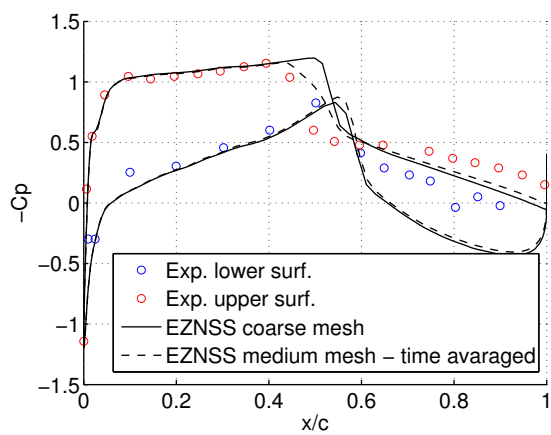
Fig. 5: Lift coefficient time history

A comparison of the computed surface pressure distribution with experimental results at the span-wise station $y/b = 0.60$ is shown in Figure 6. The results of the *SA-EC* model using the coarse grid are from the end of the time-accurate simulation, where the flow has reached a steady state. The results of the *SA-EC* model using the medium grid are based on time average over the last six flow cycles. The results of the *RSM- ω* model using the coarse grid are based on time average over the last four flow cycles.

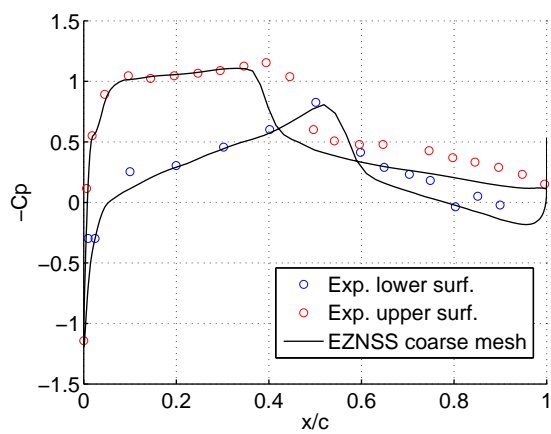
It is clear from Figure 6 that the flow prediction based on the *k- ω -TNT* model, is nearly identical for both the coarse and medium grids. The prediction of the upper shock position is downstream by approximately 10% wing chord. Moreover, the flow recovery past the shock is poorly predicted, especially on the lower wing surface. The shock prediction based on the *SA-EC* model using the coarse grid is similar to the results obtained by the *k- ω -TNT* model. The time-averaged solution based on the *SA-EC* model, using the medium grid, is in better agreement with the experimental data in terms of shock position. Still, the flow recovery prediction remains in poor agreement with the experimental results. The upper shock prediction using the *RSM- ω* model shows an opposite trend to the linear turbulence models. While the linear model predicts the shock location downstream compared to the experiment, the *RSM- ω* model predicts the shock location upstream as compared to the experimental results. The flow recovery is better predicted by the *RSM- ω*



(a) $k-\omega$ - TNT



(b) $SA-EC$



(c) $RSM-\omega$

Fig. 6: Comparison of the BSCW surface pressure coefficient at the spanwise station $y/b = 0.6$

model, especially on the lower wing surface.

2. Configuration 2 Simulations

A single Chimera computational mesh was used to study *configuration 2*. The mesh is composed of the *world* block, the splitter plate block and the wing mesh. The *world* block has the dimensions of $135 \times 101 \times 151$ and extends 100 wing chords in all directions. The splitter plate block has the dimensions of $185 \times 151 \times 151$ and is extended six wing chords in the direction of the splitter normal. The wing mesh is based on the coarse mesh that was used in *configuration 1*. The wing computational mesh was modified only in the region near the wing root, in the span-wise direction, to adjust the mesh to viscous flow conditions. The grid spacing in the two other directions was kept identical to *configuration 1*. The wing mesh has the dimensions of $253 \times 127 \times 75$ (only 75 grid point out a total 91 grid points in the normal direction were used). The wing mesh is embedded in the splitter block and the splitter block is embedded in the *world* block (see Figure 7). It is noted that the splitter is modeled as a flat plate with zero thickness. Moreover, the *world* plane mesh that lies in the wing root is treated as impermeable inviscid wall. For the study of *configuration 2* only the *SA-EC* and *RSM- ω* models were used.

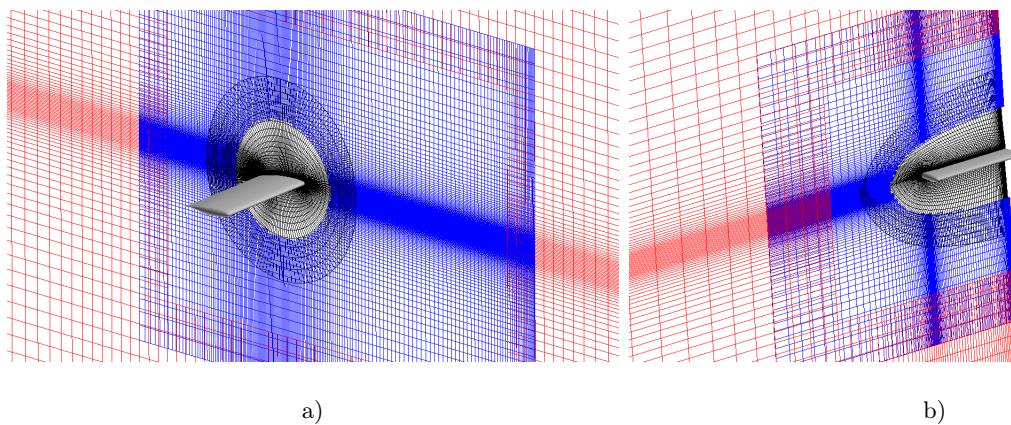


Fig. 7: BSCW *configuration 2* computational mesh;

Based on the aerodynamic force coefficients history, the simulations reached a steady state solution. Figure 8 shows the surface pressure coefficient obtained from the steady-state simulation. Excluding the wing root region and the wing tip region, there is a certain similarity between the

two solutions in terms of shock front. It was found that a forward shock position is accompanied by strong flow separation behind the shock. Moving toward the wing tip the flow becomes attached.

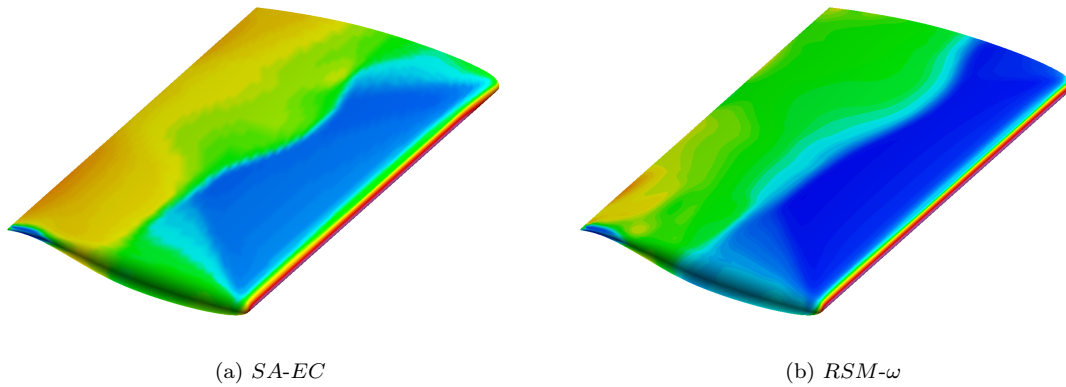


Fig. 8: BSCW surface pressure map from *configuration 2* study

A comparison of the computed surface pressure distribution with experimental results at spanwise station $y/b = 0.60$ is shown in Figure 9. Overall, the results from *configuration 2* study are in better agreement with the experimental data. Especially, the *SA-EC* model flow prediction was improved in terms of shock position and the flow recovery past the shock on the wing upper surface. The flow recovery behind the shock on the lower surface still remains in poor agreement with the experimental data.

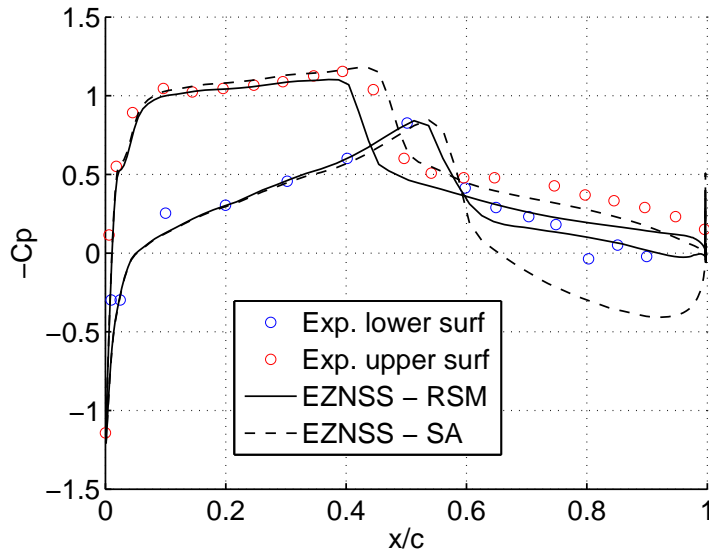


Fig. 9: Comparison of the BSCW surface pressure coefficient at the span-wise station $y/b = 0.6$ obtained from *configuration 2* study

B. High Reynolds Number Aero-Structural Dynamics (HIRENASD) Configuration

The computational mesh for the HIRENASD configuration is shown in Figure 10. It has grid zones for the wing, fuselage, a "world" zone, and a collar zone for matching flow conditions between the fuselage and wing zones. With a total of about twelve million grid points this mesh corresponds to the AePW definition of a medium mesh. Flow simulations were conducted using the HLLC scheme and the *SA-EC* turbulence model.

Static modal aeroelastic analysis is based on thirty modes of the wing only. The mode shapes, computed by MSC/Nastran modal analysis, were provided at 176 nodes along the wing, and mapped to the computational surface mesh. Figure 11 presents the first two elastic modes, on the computational surface mesh.

Static aeroelastic analysis was conducted at the flow conditions detailed in Table 1. Figures 12 - 14 present sectional surface pressure coefficient at seven span-wise sections, comparing wind-tunnel data and simulations. The computed and the wind tunnel surface pressure coefficient values are in good agreement for the ETW 250 case, as shown in Figure 12. For the ETW 132 and 129 cases there is a good match on the lower surface, and somewhat less good match on the upper surface.

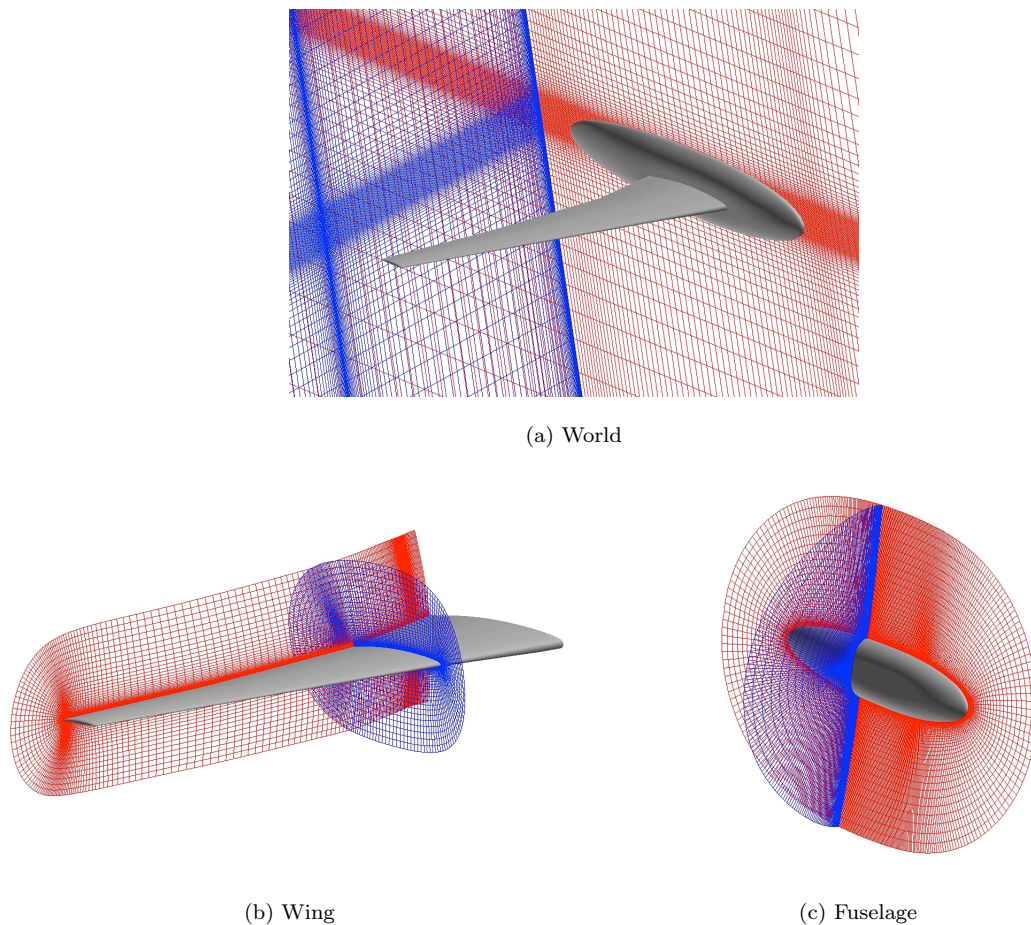


Fig. 10: HIRENASD computational mesh

Figures 15 and 16 show the transfer function (in terms of magnitude and phase angle) of the sectional C_p distributions in response to prescribed modal motion of the second bending mode at $R_\infty = 7 \times 10^6$, $M = 0.8$, about a mean angle of attack of $\alpha = 1.5^\circ$, and at dynamic pressure of $q = 40055 Pa$ (ETW 159). The frequency of the prescribed motion is $78.9 Hz$ (corresponding to the natural frequency of the second bending mode), and the excitation amplitude at the reference point ($x = 0.873, y = 1.247$) is $2.4 mm$. The later corresponds to a modal amplitude of 0.006 of the second mode. The analysis was performed using a dimensional time step of $5 \times 10^{-5} sec$, which results in about 250 time steps per cycle. The results below are based on analysis of 1500 time steps (6 cycles). Figures 15 and 16 show a reasonable agreement between the computed and wind-tunnel data. The computed magnitude of the transfer function is larger than the wind tunnel values on the upper surface for all sections. In general, the agreement is better for the lower surface than for

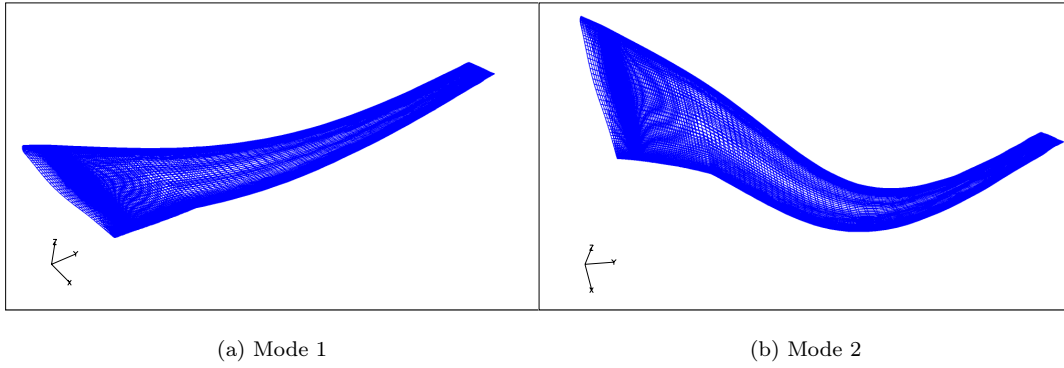


Fig. 11: HIRENASD first two elastic modes, mapped to the computational surface mesh

the upper surface.

ETW Set	$R_\infty \times 10^{-6}$	M	$\alpha [^\circ]$	$q [Pa]$
250	23.5	0.8	-1.34	88697
132	7	0.8	1.5	40055
129	7	0.7	1.5	36177

Table 1: HIRENASD flow conditions for static analysis

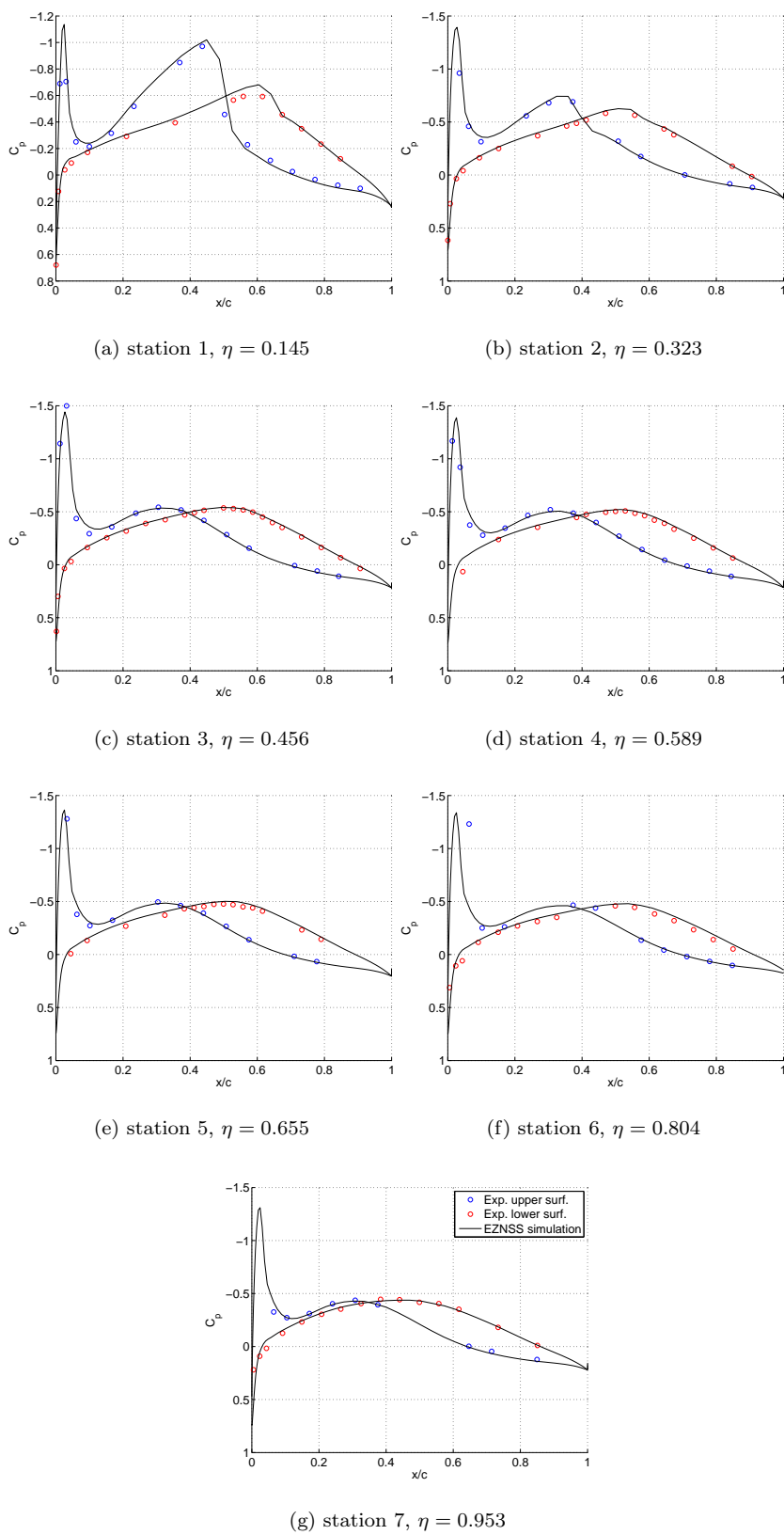


Fig. 12: HIRENASD sectional C_p ; $R_\infty = 23.5 \times 10^6$, $M = 0.8$, $\alpha = -1.34^\circ$, $q = 88697 Pa$, ETW

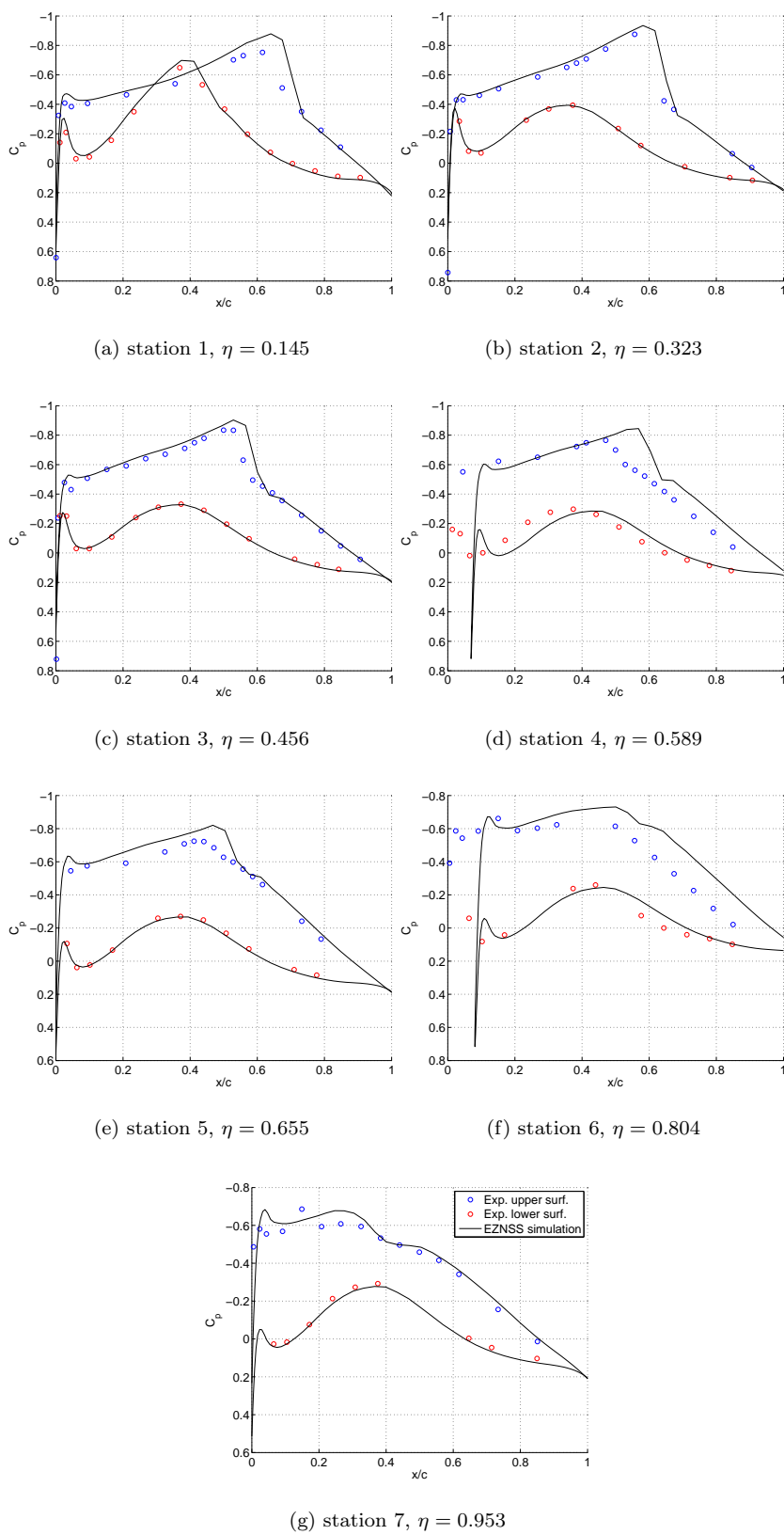


Fig. 13: HIRENASD sectional C_p ; $R_\infty = 7 \times 10^6$, $M = 0.8$, $\alpha = 1.5^\circ$, $q = 40055 Pa$, ETW 132

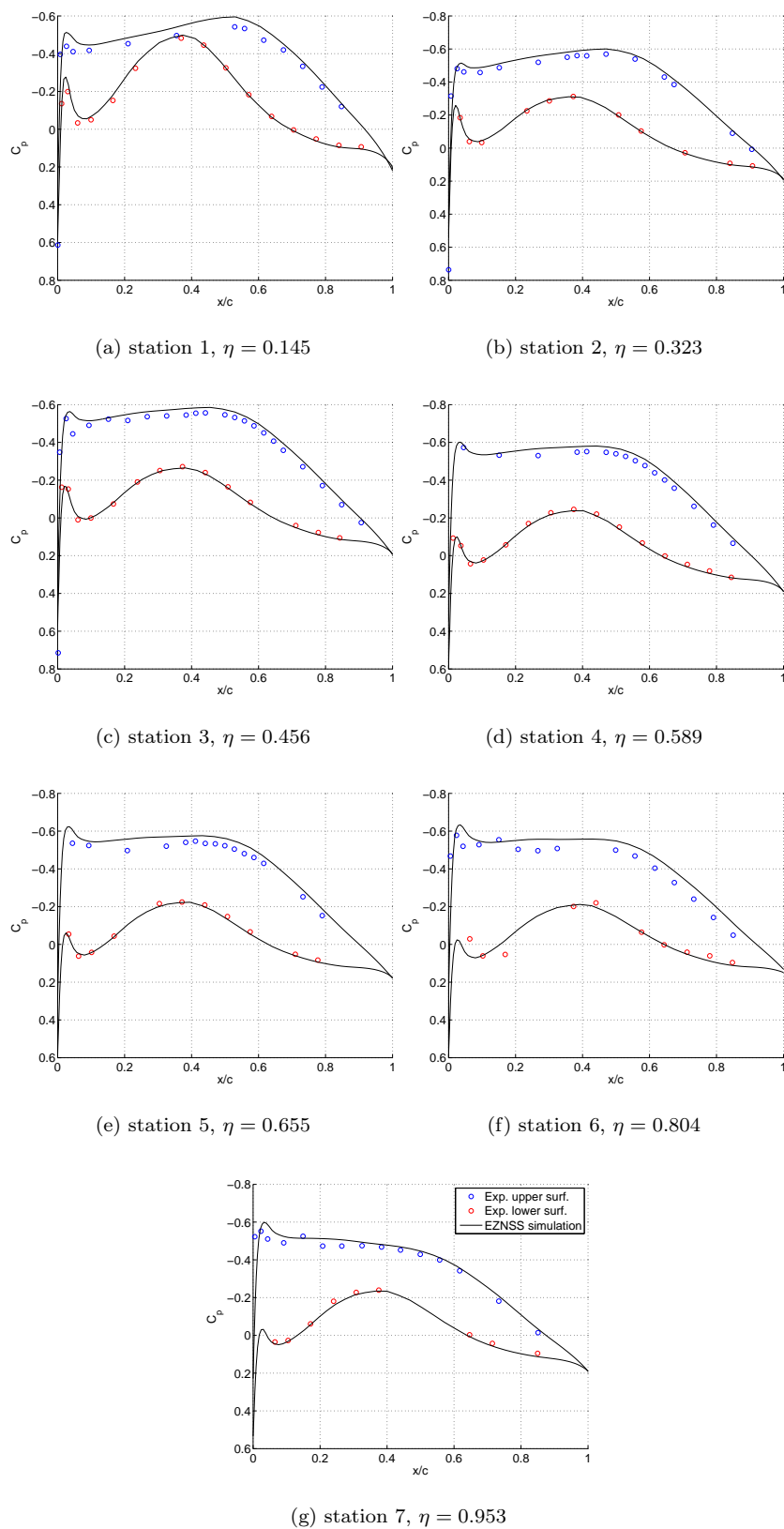


Fig. 14: HIRENASD sectional C_p ; $R_\infty = 7 \times 10^6$, $M = 0.7$, $\alpha = 1.5^\circ$, $q = 36177 Pa$, ETW 129

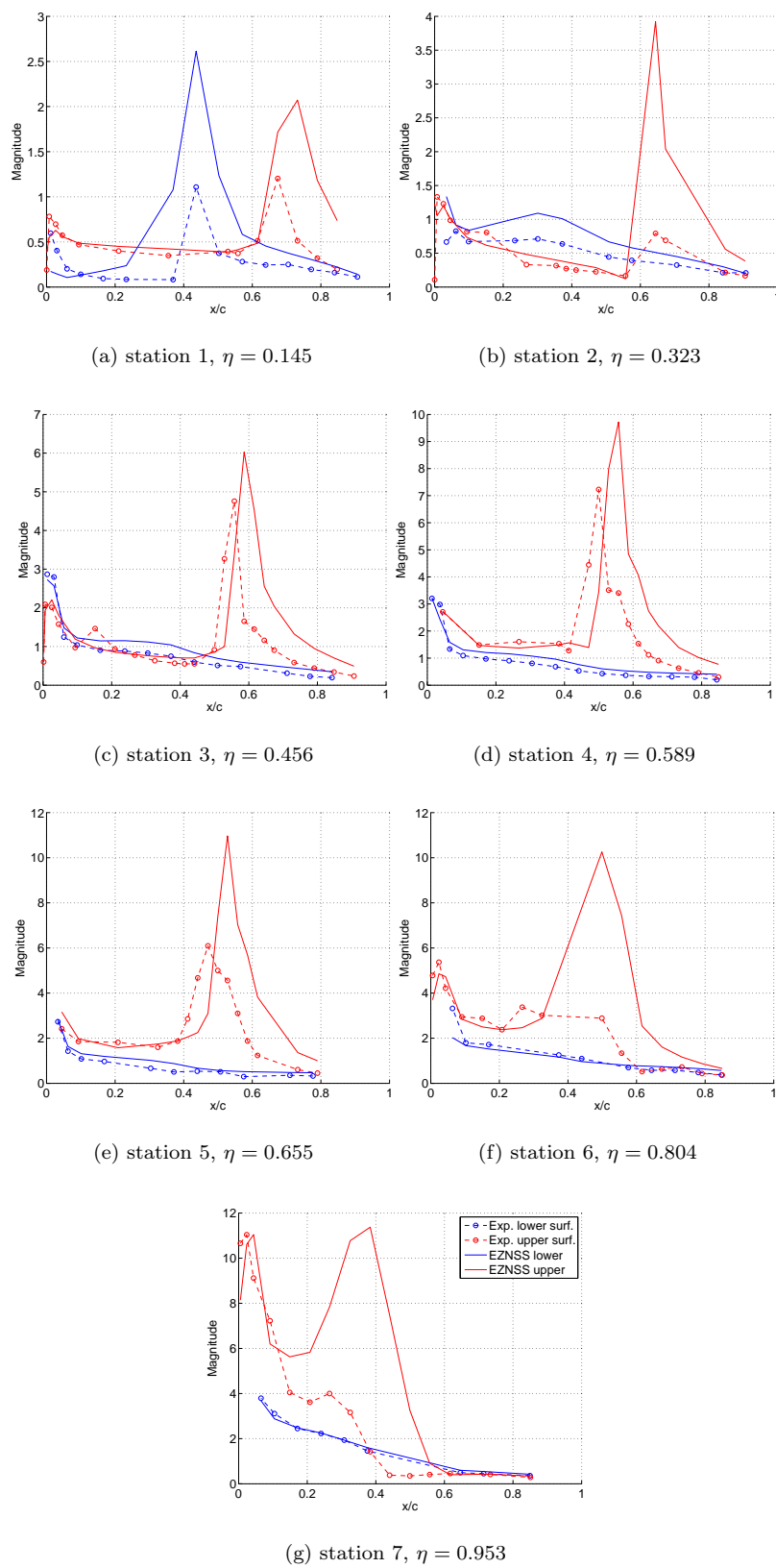


Fig. 15: HIRENASD C_p response to prescribed excitation - magnitude; $R_\infty = 7 \times 10^6$, $M = 0.8$,

$$\alpha = 1.5^\circ, q = 40055 Pa, \text{ ETW 159}$$

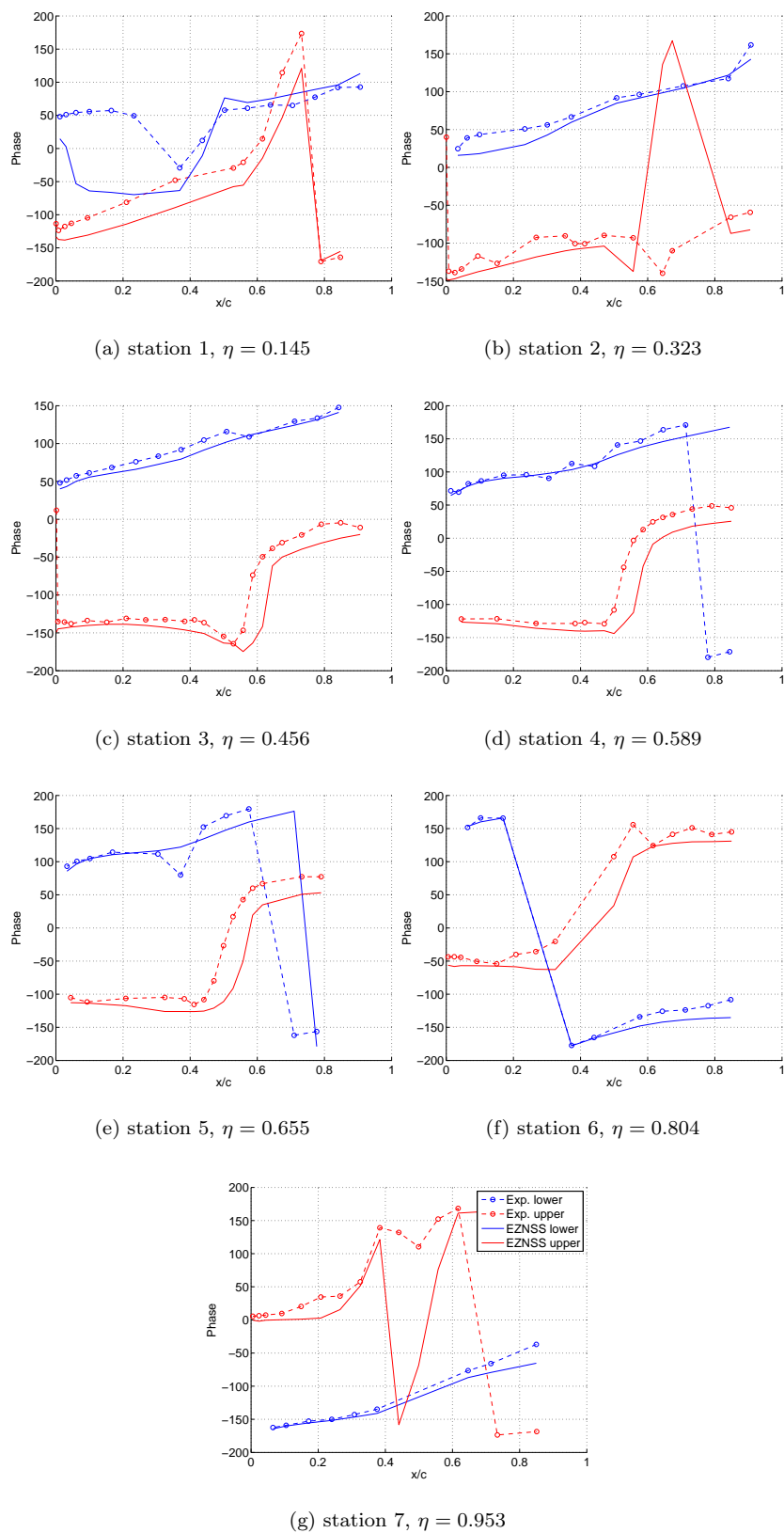


Fig. 16: HIRENASD C_p response to prescribed excitation - phase; $R_\infty = 7 \times 10^6$, $M = 0.8$,

$$\alpha = 1.5^\circ, q = 40055 Pa, \text{ ETW 159}$$

V. Summary

Numerical simulations were performed with the EZNSS flow solver for the first NASA Langley Aeroelastic Prediction Workshop. Two configurations were studied, the Benchmark Supercritical Wing (BSCW) and the High Reynolds Number Aerostructural Dynamics (HIRENASD) model. Two geometrical configurations of the BSCW were examined and 3 turbulence models were utilized. All of the models predicted the shock location within 10% chords of its wind-tunnel location. None of the models predicted accurately the pressure recovery behind the shock on the upper and lower surfaces. While some turbulence models and computational setups resulted in a steady flow, some predicted flow unsteadiness, with fluctuations of the shock position and of the aerodynamic coefficient values. This may indicate that the case of the BSCW wing, at the studied flow conditions, is on the verge of buffet instability. A grid study, using a coarse and medium meshes, showed that the results are sensitive to the grid density. Another configuration introduced a viscously modeled splitter plate, which appears to somewhat improve the pressure distribution prediction.

The HIRENASD wing was studied for its elastic deformations and associated pressure coefficient distribution at three flow conditions of various Reynolds numbers, Mach numbers, and mean angle of attack. All of the studied flow conditions resulted in good correlation between the computed and experimental pressure coefficient data. The HIRENASD wing was also excited at its second-bending mode. The transfer function between the pressure coefficient distribution at different span-wise sections and the amplitude of motion of a reference point was computed and compared to experimental data. A fair comparison was demonstrated.

Overall, it appears that the numerical simulations predicted well the transonic static aeroelastic response and the response to forced excitation in cases of attached flows. The transonic cases of detached flows behind a shock were found to be highly sensitive to the numerical parameters of the simulation, especially the turbulence model used. Due to these observations, and due to the lack of experimental data on three-dimensional wing in buffet conditions, it is recommended that one of the next Aeroelastic Prediction Workshops will target shock buffet experiments and simulations.

VI. References

- [1] J. Heeg, J. Ballman, K. Bhatia, E. Blades, A. Boucke, P. Chwalowski, G. Dietz, E. Dowell, J. Florance, T. Hansen, M. Mani, D. Mavriplis, B. Perry, M. Ritter, D. Schuster, M. Smith, P. Taylor, B. Whiting, and C. Wieseman. Plans for the Aeroelastic Prediction Workshop. In *International Forum on Aeroelasticity and Structural Dynamics*, Paris, June 2011. IFASD-2011-999.
- [2] C. Kok, Johan. Resolving the dependence on freestream values for the k- ω turbulence model. *AIAA Journal*, 38(7):1292–1295, 2000.
- [3] Jack R. Edwards and Suresh Chandra. Comparison of eddy viscosity-transport turbulence models for three-dimensional, shock-separated flow fields. *AIAA Journal*, 34(4):756–763, 1996.
- [4] D. C. Wilcox. *Turbulence modeling for CFD (Third edition)*. DCW Industries, Inc. 5354 Palm Drive, La Canada, California 91011, 2006.
- [5] B. J. Daly and F. H. Harlow. Transport equations in turbulence. *Physics of Fluids*, 13(11):2634–2649, 1970.
- [6] P. Batten, M. A. Leschziner, and U. C. Goldberg. Average-state Jacobians and implicit methods for compressible viscous and turbulent flows. *Journal of Computational Physics*, 137(1):38–78, 1997.
- [7] Meng-Sing Liou. A sequel to AUSM, part II:AUSM⁺-up for all speeds. *Journal of Computational Physics*, 214(1):137–170, 2006.
- [8] G. H. Klopfer, R. F. Van der Wijngaart, C. M. Hung, and J. T. Onufer. A diagonalized diagonal dominant alternating direction implicit (D3ADI) scheme and subiteration correction. In *29th Fluid Dynamics Conference*, Albuquerque, NM, June 1998. AIAA paper 1998 - 2824.
- [9] Y. Mor-Yossef and Y. Levy. The unconditionally positive-convergent implicit time integration scheme for two-equation turbulence models: Revisited. *Computers & Fluids*, 38(10):1984–1994, 2009.
- [10] Y. Mor-Yossef and Y. Levy. Designing a positive second-order implicit time integration procedure for unsteady turbulent flows. *Computer Methods in Applied Mechanics and Engineering*, 196(41-44):4196–4206, 2007.
- [11] Harder R. L. and Desmarais R. N. Interpolation Using Surface Splines. *Journal of Aircraft*, 9(2):189–191, 1972.
- [12] Raveh D. E., Levy Y., and Karpel M. Structural Optimization Using Computational Aerodynamics. *Journal of Aircraft*, 38(10):1974–1982, 2000.
- [13] Schuster D. M. Vadyak J. and Atta E. Static Aeroelastic Analysis of Fighter Aircraft Using a Three-Dimensional Navier-Stokes Algorithm. *Journal of Aircraft*, 27(5):820–825, 1990.